PAPER

Enhanced Universal Filtered-DFTs-OFDM for Long-Delay Multipath Environment

Yuji MIZUTANI[†a)], *Nonmember*, **Hiroto KURIKI**[†], *Member*, **Yosuke KODAMA**[†], *Nonmember*, **Keiichi MIZUTANI**[†], **Takeshi MATSUMURA**[†], *Members*, *and* **Hiroshi HARADA**[†], *Fellow*

SUMMARY The conventional universal filtered-DFT-spread-OFDM (UF-DFTs-OFDM) can drastically improve the out-of-band emission (OOBE) caused by the discontinuity between symbols in the conventional cyclic prefix-based DFTs-OFDM (CP-DFTs-OFDM). However, the UF-DFTs-OFDM degrades the communication quality in a long-delay multipath fading environment due to the frequency-domain ripple derived from the long transition time of the low pass filter (LPF) corresponding to the guard interval (GI). In this paper, we propose an enhanced UF-DFTs-OFDM (eUF-DFTs-OFDM) that achieves significantly low OOBE and high communication quality even in a long-delay multipath fading environment. The eUF-DFTs-OFDM applies an LPF with quite short length in combination with the zero padding (ZP) or the CP process. Then, the characteristics of the OOBE, peak-to-average power ratio (PAPR), and block error rate (BLER) are evaluated by computer simulation with the LTE uplink parameters. The result confirms that the eUF-DFTs-OFDM can improve the OOBE by 22.5 dB at the channel-edge compared to the CP-DFTs-OFDM, and also improve the E_S/N_0 to achieve BLER = 10^{-3} by about 2.5 dB for QPSK and 16QAM compared to the UF-DFTs-OFDM. For 64QAM, the proposed eUF-DFTs-ODFDM can eliminate the error floor of the UF-DFTs-OFDM. These results indicate that the proposed eUF-DFTs-OFDM can significantly reduce the OOBE while maintaining the same level of communication quality as the CP-DFTs-OFDM even in long-delay multipath environment.

key words: *CP-DFTs-OFDM, UF-DFTs-OFDM, long-delay multipath fading environment, LTE, beyond 5G*

1. Introduction

In recent years, data traffic in mobile cellular systems has dramatically increased due to the demands being placed on sophisticated mobile network services and applications for smartphones [1]. Furthermore, responding to the emergence of all-new Internet of things (IoT)-based use cases including self-driving and telemedicine, enhanced mobile broadband (eMBB), ultra-reliable and low latency communications (URLLC), and massive machine type communication (mMTC) will be supported in the upcoming 5th generation mobile communication (5G) and beyond [2]–[5]. In addition, the 5G and beyond will form more versatile heterogeneous wireless networks where various radio access systems are densely and simultaneously operated in the same area to cope with a variety of applications. Therefore, the development of physical layer waveforms [6]–[17] that can reduce interferences among systems is one of the most important objectives in improving the overall spectrum efficiency.

In existing LTE system, the cyclic prefix (CP)-based discrete Fourier transform (DFT)-spread OFDM (CP-DFTs-OFDM) is applied as an uplink multiplexing scheme because of its low peak-to-average power ratio (PAPR) [18]. CP-DFTs-OFDM contributes to high communication quality by mitigating the effect of the multipath fading, while unfortunately creating high out-of-band emission (OOBE) due to the discontinuity between successive symbols [19]. Therefore, a variety of new-waveforms have been investigated for suppressing the OOBE effectively [6]–[17]. The universal filtered (UF)-DFTs-OFDM has been also proposed as a new-waveform based on the DFTs-OFDM [8]. The conventional UF-DFTs-OFDM can improve the OOBE drastically by dividing subcarriers into some sub-bands and applying a low pass filter (LPF) to each sub-band in time-domain. However, the transition time of the LPF used as the guard interval (GI) should be extended in a long-delay multipath environment, causing a large frequency-domain ripple that degrades the communication quality.

In this paper, we propose an enhanced UF-DFTs-OFDM (eUF-DFTs-OFDM) that offers significantly low OOBE while maintaining high communication quality even in a long-delay multipath environment [9]. The proposed eUF-DFTs-OFDM applies the LPF with short transition time in combination with the zero padding (ZP) or the CP [9] to suppress the frequency-domain ripple and to mitigate the effect of multipath fading. This proposed scheme is based on the enhanced UF-OFDM (eUF-OFDM) [10], [11] previously proposed by the authors and the flexible CP-OFDM (FCP-OFDM) [12] proposed shortly thereafter. These schemes can suppress the OOBE without degrading communication quality in the 3GPP Extended Typical Urban (ETU) channel model [20] but still has high PAPR of the transmission signal as well as the conventional CP-OFDM and the UF-OFDM. Meanwhile, the proposed eUF-DFTs-OFDM can reduce PAPR to the same level as the conventional CP-DFTs-OFDM because of the application of DFT spreading. With the comprehensive evaluation using computer simulation on OOBE, PAPR, and block error rate (BLER) with the LTE uplink parameters in the 3GPP ETU channel model, we demonstrate that the proposed eUF-DFTs-OFDM achieves significant OOBE reduction with maintaining satisfactory communication quality and low PAPR in a long-delay multipath environment.

The rest of this paper is organized as follows. An

Manuscript received February 14, 2019.
Manuscript revised June 9, 2019.
Manuscript publicized October 8, 2019.

[†]The authors are with Kyoto University, Kyoto-shi, 606-8501 Japan.
a) E-mail: contact@dco.cce.i.kyoto-u.ac.jp

DOI: 10.1587/transcom.2019EBP3044

overview of the conventional UF-DFTs-OFDM is described in Sect. 2. Then, the ZP-based and CP-based eUF-DFTs-OFDM are proposed in Sect. 3. In Sect. 4, performances of the proposed eUF-DFTs-OFDM are evaluated comprehensively by computer simulation using the LTE uplink parameters. Finally, we conclude this paper in Sect. 5.

2. Conventional UF-DFTs-OFDM

2.1 Transmitter Architecture

Figure 1 shows the transmission process of the UF-DFTs-OFDM. Firstly, after mapping the modulated symbols to physical resource block (PRB), M-by-M size DFT is executed to the modulated symbol vector of the k-th OFDM symbol $\boldsymbol{a}_k = [a_{(k,0)}, a_{(k,1)}, \ldots, a_{(k,M-1)}]^{\mathrm{T}} \in \mathbb{C}^{M\times 1}$ and $\boldsymbol{a}_k$ is converted into the subcarrier vector of the k-th DFTs-OFDM symbol $\boldsymbol{z}_k = [z_{(k,0)}, z_{(k,1)}, \ldots, z_{(k,M-1)}]^{\mathrm{T}} \in \mathbb{C}^{M\times 1}$. Here, M represents the number of modulated symbols included in one DFTs-OFDM symbol, and $a_{(k,n)}$ and $z_{(k,n)}$ denote the n-th modulated symbol of the k-th OFDM symbol and the n-th subcarrier of the k-th DFTs-OFDM symbol, respectively. This DFT-spreading process can be executed as follows:

$$\boldsymbol{z}_{\boldsymbol{k}} = \boldsymbol{F}_{(M,M)}\boldsymbol{a}_k, \tag{1}$$

$$\left(\boldsymbol{F}_{(A,B)}\right)_{p_1,p_2} = \exp\left[-\mathrm{j}2\pi p_1 p_2/A\right], \tag{2}$$

where $0 \le p_1 < A$ and $0 \le p_2 < B$, and $\boldsymbol{F}_{(A,B)} \in \mathbb{C}^{A\times B}$ denotes the A-by-B size DFT matrix. Secondly, subcarriers are divided into B sub-bands. Figure 2 shows the generation process of the transmission symbol after the IDFT process. Here, each sub-band contains M_0 subcarriers (i.e., $B = M/M_0$). Consequently, $\boldsymbol{z}_k^i \in \mathbb{C}^{M_0\times 1}$ $(0 \le i < B)$ corresponding to the i-th sub-band of the k-th DFTs-OFDM symbol can be expressed as follows:

$$\boldsymbol{z}_{\boldsymbol{k}} = \left[\left(\boldsymbol{z}_k^0\right)^{\mathrm{T}}, \left(\boldsymbol{z}_k^1\right)^{\mathrm{T}}, \ldots, \left(\boldsymbol{z}_k^{B-1}\right)^{\mathrm{T}}\right]^{\mathrm{T}}, \tag{3}$$

$$\boldsymbol{z}_k^i = \left[z_{(k,iM_0)}, z_{(k,iM_0+1)}, \ldots, z_{(k,(i+1)M_0-1)}\right]^{\mathrm{T}}. \tag{4}$$

After dividing subcarriers into B sub-bands, N_{FFT}-by-M_0 size inverse DFT (IDFT) is executed to $\boldsymbol{z}_k^i$ and the k-th DFTs-OFDM symbol of the i-th sub-band $\boldsymbol{s}_k^i \in \mathbb{C}^{N_{\mathrm{FFT}}\times 1}$ can be obtained as follows:

$$\boldsymbol{s}_k^i = \left(F^i_{(N_{\mathrm{FFT}},M_0)}\right)^{-1}\boldsymbol{z}_k^i, \tag{5}$$

$$\left(\boldsymbol{F}^i_{(A,B)}\right)^{-1}_{p_1,p_2} = \exp\left[\mathrm{j}2\pi(iM_0 + p_2)p_1/A\right], \tag{6}$$

where $0 \le p_1 < A$ and $0 \le p_2 < B$, and $\left(\boldsymbol{F}^i_{(A,B)}\right)^{-1} \in \mathbb{C}^{A\times B}$ represents the A-by-B size IDFT matrix corresponding to the i-th sub-band. Subsequently, the LPF with a length of L_{F} is applied to each sub-band (Fig. 2(b)). Note that $L_{\mathrm{F}}-1$ is equal to the CP length of CP-DFTs-OFDM L_{CP} [13], and thus, length of the k-th UF-DFTs-OFDM symbol is same as that of CP-DFTs-OFDM symbol. The frequency characteristics of the LPF is adjusted corresponding to the center frequency of each sub-band. When the impulse response of the LPF is

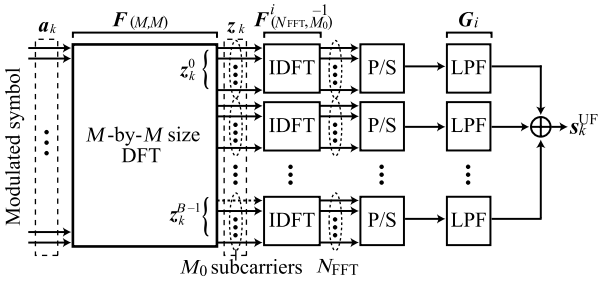

Fig. 1 Transmission process of UF-DFTs-OFDM.

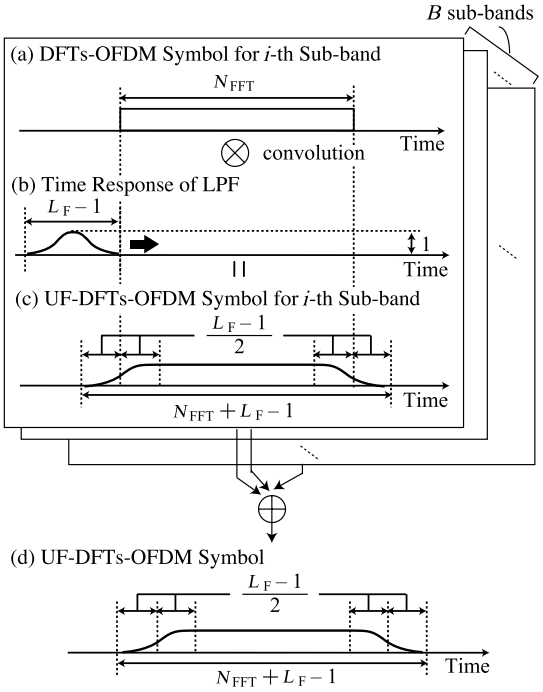

Fig. 2 Generation process of transmission symbol in UF-DFTs-OFDM.

defined as $g(n)$ $(0 \le n < L_{\mathrm{F}})$, the impulse response in the i-th sub-band $g_i(n)$ is given by

$$g_i(n) = g(n)\exp\left[\mathrm{j}2\pi m_i^{\mathrm{c}}/N_{\mathrm{FFT}}\right], \tag{7}$$

where $m_i^{\mathrm{c}} = (M_0+1)/2 + (i-1)M_0$ represents the subcarrier index at the center of the i-th sub-band. Therefore, the LPF can be convoluted in time-domain with the following Toeplitz matrix $\boldsymbol{G}_i \in \mathbb{C}^{(N_{\mathrm{FFT}}+L_{\mathrm{CP}})\times N_{\mathrm{FFT}}}$ that satisfies the following conditions:

$$(\boldsymbol{G}_i)_{p,0} = \begin{cases} g_i(p) & (0 \le p < L_{\mathrm{F}}) \\ 0 & (L_{\mathrm{F}} \le p < N_{\mathrm{FFT}} + L_{\mathrm{CP}}) \end{cases}, \tag{8}$$

$$(\boldsymbol{G}_i)_{0,q} = \begin{cases} g_i(0) & (q = 0) \\ 0 & (q \ne 0) \end{cases}, \tag{9}$$

$$(\boldsymbol{G}_i)_{p,q} = (\boldsymbol{G}_i)_{p-1,q-1} \ (p \ne 0, q \ne 0). \tag{10}$$

Then, transmission symbols of the UF-DFTs-OFDM are obtained by the summation of the time-domain symbols in all sub-bands (Fig. 2(d)). Therefore, the k-th UF-DFTs-OFDM

symbol $\boldsymbol{s}_k^{\mathrm{UF}} \in \mathbb{C}^{(N_{\mathrm{FFT}}+L_{\mathrm{CP}})\times 1}$ can be expressed by using a matrix $\boldsymbol{J}_i^{\mathrm{UF}}$ $(= \boldsymbol{G}_i \left(\boldsymbol{F}^i_{(N_{\mathrm{FFT}},M_0)}\right)^{-1}) \in \mathbb{C}^{(N_{\mathrm{FFT}}+L_{\mathrm{CP}})\times M_0}$ as follows:

$$\boldsymbol{s}_k^{\mathrm{UF}} = \sum_{i=0}^{B-1} \boldsymbol{J}_i^{\mathrm{UF}} \boldsymbol{z}_k^i. \tag{11}$$

Finally, serial transmission symbols can be obtained by concatenating successive UF-DFTs-OFDM symbols $\boldsymbol{s}_k^{\mathrm{UF}}$. Here, the rise and fall time of the LPF in time-domain are used as the GI. In the UF-DFTs-OFDM, the frequency-domain ripple caused by the LPF can be compensated by a predistortion (PD) process because characteristics of the ripple depend on only transmission symbol parameters and can be calculated at the transmitter in advance. The detail of this PD process is explained in Sect. 2.3.

2.2 Receiver Architecture

Figure 3 shows the reception process of the UF-DFTs-OFDM. In the general case of a relaxed synchronization scenario where there are interferences from other asynchronous users using neighboring spectrum resources, the k-th reception symbol $\boldsymbol{r}_k^{\mathrm{UF}} \in \mathbb{C}^{(N_{\mathrm{FFT}}+L_{\mathrm{CP}})\times 1}$ is multiplied by a time window to suppress inter-user interferences. However, this relaxed synchronization scenario is not assumed in this paper, and this time-domain process is omitted. After the time-domain process, the received UF-DFTs-OFDM symbol $\boldsymbol{r}_k^{\mathrm{UF}}$ is zero-padded since its length is $N_{\mathrm{FFT}} + L_{\mathrm{CP}}$. Then, $2N_{\mathrm{FFT}}$-points fast Fourier transform (FFT) is performed and M subcarriers in the allocated band are extracted. Therefore, the received subcarriers (i.e., input frequency-domain subcarriers to channel equalizer) $\boldsymbol{y}_k^{\mathrm{UF}} = [\boldsymbol{y}_{(k,1)}^{\mathrm{UF}}, \boldsymbol{y}_{(k,2)}^{\mathrm{UF}}, \ldots, \boldsymbol{y}_{(k,M)}^{\mathrm{UF}}]^{\mathrm{T}} \in \mathbb{C}^{M\times 1}$ can be expressed as follows:

$$\boldsymbol{y}_k^{\mathrm{UF}} = \boldsymbol{R}_{\mathrm{UF}} \boldsymbol{r}_k^{\mathrm{UF}}, \tag{12}$$

$$\boldsymbol{R}_{\mathrm{UF}} = \boldsymbol{Q}'_M \boldsymbol{F}_{(2N_{\mathrm{FFT}},2N_{\mathrm{FFT}})} \boldsymbol{S}_{\mathrm{ZP}}^{(N_{\mathrm{FFT}}+L_{\mathrm{CP}},N_{\mathrm{FFT}}-L_{\mathrm{CP}})}, \tag{13}$$

$$\boldsymbol{S}_{\mathrm{ZP}}^{(N_{\mathrm{S}},N_{\mathrm{Z}})} = \begin{bmatrix} \boldsymbol{I}^{N_{\mathrm{S}}\times N_{\mathrm{S}}} \\ \boldsymbol{0}^{N_{\mathrm{Z}}\times N_{\mathrm{S}}} \end{bmatrix}, \tag{14}$$

$$(\boldsymbol{Q}'_M)_{p,q} = \begin{cases} 1 \ (p = k, q = 2k-1) \\ 0 \ (\text{other}) \end{cases}, \tag{15}$$

where $\boldsymbol{I}^{N_{\mathrm{S}}\times N_{\mathrm{S}}} \in \mathbb{Z}^{N_{\mathrm{S}}\times N_{\mathrm{S}}}$ and $\boldsymbol{0}^{N_{\mathrm{Z}}\times N_{\mathrm{S}}} \in \mathbb{Z}^{N_{\mathrm{Z}}\times N_{\mathrm{S}}}$ denote a N_{S}-by-N_{S} size unit matrix and a N_{Z}-by-N_{S} zero matrix, respectively, and $\boldsymbol{S}_{\mathrm{ZP}}^{(N_{\mathrm{S}},N_{\mathrm{Z}})} \in \mathbb{C}^{(N_{\mathrm{S}}+N_{\mathrm{Z}})\times N_{\mathrm{S}}}$ denotes the zero-padding process. Furthermore, $1 \le k \le M$, $k \in \mathbb{N}$, and

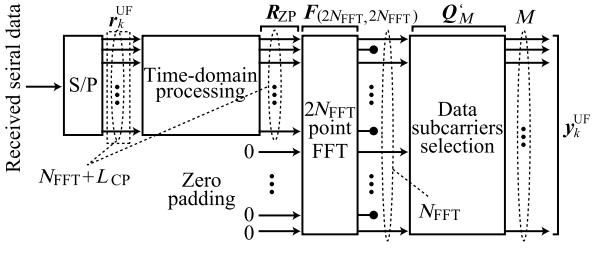

Fig. 3 Reception process of UF-DFTs-OFDM.

$\boldsymbol{Q}'_M \in \mathbb{C}^{M\times 2N_{\mathrm{FFT}}}$ denotes the extraction of the allocated M subcarriers. Finally, after the frequency-domain equalization (FDE) by the minimum mean square error (MMSE) filter, the received bit sequence can be obtained by the inverse process of the transmitter.

2.3 Pre-Distortion Process for UF-DFTs-OFDM

In this section, the details of the PD process for the UF-DFTs-OFDM is explained. A ripple coefficient of the UF-DFTs-OFDM can be calculated according to the following procedure. Firstly, B sub-bands with an amplitude of 1 $\boldsymbol{1}^{M_0\times 1} \in \mathbb{Z}^{M_0\times 1}$ are prepared and the wave-shaping for the UF-DFTs-OFDM is executed to these sub-bands. Here, $\boldsymbol{1}^{A\times B} \in \mathbb{Z}^{A\times B}$ represents the A-by-B size matrix in which all coefficients are 1. Also, this wave-shaping process for the i-th sub-band can be executed by the matrix $\boldsymbol{J}_i^{\mathrm{UF}}$. Subsequently, the reception process is executed to the wave-shaped time-domain signal, and ripple coefficient vector $\boldsymbol{h}^{\mathrm{UF}} = [h_1^{\mathrm{UF}}, h_2^{\mathrm{UF}}, \ldots, h_M^{\mathrm{UF}}]^{\mathrm{T}} \in \mathbb{C}^{M\times 1}$ can be obtained as follows:

$$\boldsymbol{h}^{\mathrm{UF}} = \frac{1}{N}\left[\sum_{i=0}^{B-1} R_{\mathrm{UF}} \boldsymbol{J}_i^{\mathrm{UF}} \boldsymbol{1}^{M_0\times 1}\right]^{\mathrm{T}}, \tag{16}$$

where N denotes normalization factor by the mean value of ripple coefficients, and R_{UF} is defined by Eq. (13). Therefore, when $\boldsymbol{h}_{\mathrm{inv}}^{\mathrm{UF}}$ is defined as a vector $[1/h_1^{\mathrm{UF}}, 1/h_2^{\mathrm{UF}}, \ldots, 1/h_M^{\mathrm{UF}}]^{\mathrm{T}} \in \mathbb{C}^{M\times 1}$, the PD process can be executed by the multiplication of $\boldsymbol{z}_k$ and the following diagonal matrix $\boldsymbol{H}_{\mathrm{LPF}}^{\mathrm{UF}} \in \mathbb{C}^{M\times M}$ in which diagonal elements are $\boldsymbol{h}_{\mathrm{inv}}^{\mathrm{UF}}$:

$$\boldsymbol{H}_{\mathrm{LPF}}^{\mathrm{UF}} = \mathrm{diag}(\boldsymbol{h}_{\mathrm{inv}}^{\mathrm{UF}}), \tag{17}$$

where $\mathrm{diag}(\boldsymbol{x}) \in \mathbb{C}^{A\times A}$ denotes the diagonal matrix in which diagonal elements are vector $\boldsymbol{x} \in \mathbb{C}^{A\times 1}$. Therefore, in the case of the UF-DFTs-OFDM wave-shaping with the PD process $\boldsymbol{z}_k$ should be replaced with $\hat{\boldsymbol{z}}_k = \boldsymbol{H}_{\mathrm{LPF}}^{\mathrm{UF}} \boldsymbol{z}_k$ in Eq. (3).

2.4 Problem in Long-Delay Multipath Environment

In the case of the UF-DFTs-OFDM, the effective GI length of the UF-DFTs-OFDM becomes $(L_{\mathrm{F}} - 1)/2$ that is half of the CP length of the CP-DFTs-OFDM. In several papers, the LTE parameters of the normal CP mode are applied to the UF-DFTs-OFDM evaluation (i.e., CP length = 4.7 μs, and $L_{\mathrm{F}} = 37$ when the sampling frequency is 7.68 MHz) [17]. In this case, the effective GI length of the UF-DFTs-OFDM becomes 4.7 μs/2 = 2.35 μs. Obviously, short effective GI length reduces a margin for the transmission delay, and thus, the LPF length should be extended in a long-delay multipath environment. In the LTE specification, we can select the extended CP mode (i.e., CP length = 16.7 μs). Therefore, to operate the UF-DFTs-OFDM-based system under long-delay multipath environment such as the 3GPP ETU channel model [20], the transition time of the LPF for the UF-DFTs-OFDM should be set to the same as the CP length of the extended CP mode of LTE (i.e., $L_{\mathrm{F}} = 129$

when the sampling frequency is 7.68 MHz). However, due to the large frequency-domain ripple caused by the LPF with long length, the amplitude of some subcarriers becomes extremely low. Such a low received signal level lessens the signal-to-noise ratio (SNR) in these subcarriers and significantly degrades communication quality.

3. Proposed eUF-DFTs-OFDM

To improve the drawback of the UF-DFTs-OFDM, eUF-DFTs-OFDM is proposed [9]. The proposed eUF-DFTs-OFDM is sufficiently robust against long-delay multipath fading by combining the ZP or the CP with LPF that has a quite shorter length than the UF-DFTs-OFDM (i.e., the ZP-eUF-DFTs-OFDM and the CP-eUF-DFTs-OFDM [9], respectively).

3.1 Proposed ZP-eUF-DFTs-OFDM

3.1.1 Transmitter Architecture

Figure 4 shows the transmitter architecture of the proposed ZP/CP-eUF-DFTs-OFDM, and Fig. 5 shows the generation process of the proposed ZP-eUF-DFTs-OFDM symbol in each sub-band. In the proposed ZP-eUF-DFTs-OFDM, the ZP is added to the transmission process of the UF-DFTs-OFDM. Firstly, after the time-domain waveform $\boldsymbol{s}_k^i$ is generated by following the same processes of the UF-DFTs-OFDM, zeros with a length of L'_{CP} ($= L_{\mathrm{CP}} - L_{\mathrm{F}} + 1$) is suffixed to $\boldsymbol{s}_k^i$ before applying the LPF in each sub-band (Fig. 5(a)). This ZP process in each sub-band can be executed by the matrix $\boldsymbol{S}_{\mathrm{ZP}}^{(N_{\mathrm{FFT}},L'_{\mathrm{CP}})} \in \mathbb{C}^{(N_{\mathrm{FFT}}+L'_{\mathrm{CP}})\times N_{\mathrm{FFT}}}$. After the ZP process, the LPF is applied to the ZP-DFTs-OFDM symbols (Fig. 5(b)). The LPF convolution in time-domain is executed by the Toepliz matrix $\boldsymbol{G}_i \in \mathbb{C}^{(N_{\mathrm{FFT}}+L_{\mathrm{CP}})\times(N_{\mathrm{FFT}}+L'_{\mathrm{CP}})}$ that satisfies the conditions of Eqs. (8)–(10). Then, time-domain symbols in all sub-bands are summed, and thus, the k-th ZP-eUF-DFTs-OFDM symbol $\boldsymbol{s}_k^{\mathrm{ZP(eUF)}} \in \mathbb{C}^{(N_{\mathrm{FFT}}+L_{\mathrm{CP}})\times 1}$ can be expressed by using the matrix $\boldsymbol{J}_i^{\mathrm{ZP(eUF)}}$ ($= \boldsymbol{G}_i \boldsymbol{S}_{\mathrm{ZP}}^{(N_{\mathrm{FFT}},L'_{\mathrm{CP}})} (\boldsymbol{F}^i_{(N_{\mathrm{FFT}},M_0)})^{-1}$) $\in \mathbb{C}^{(N_{\mathrm{FFT}}+L_{\mathrm{CP}})\times M_0}$ as follows:

$$\boldsymbol{s}_k^{\mathrm{ZP(eUF)}} = \sum_{i=0}^{B-1} \boldsymbol{J}_i^{\mathrm{ZP(eUF)}} \boldsymbol{z}_k^i. \tag{18}$$

Finally, transmission symbol of the proposed ZP-eUF-DFTs-OFDM can be obtained by concatenating successive symbols $\boldsymbol{s}_k^{\mathrm{ZP(eUF)}}$.

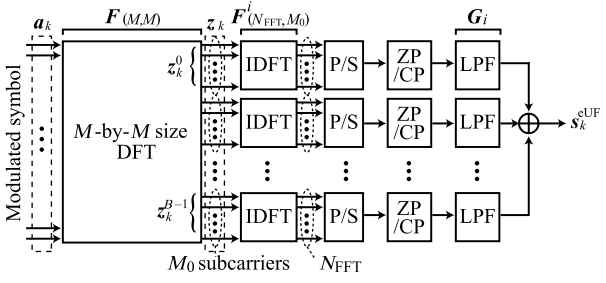

Fig. 4 Transmission process of proposed ZP/CP-eUF-DFTs-OFDM.

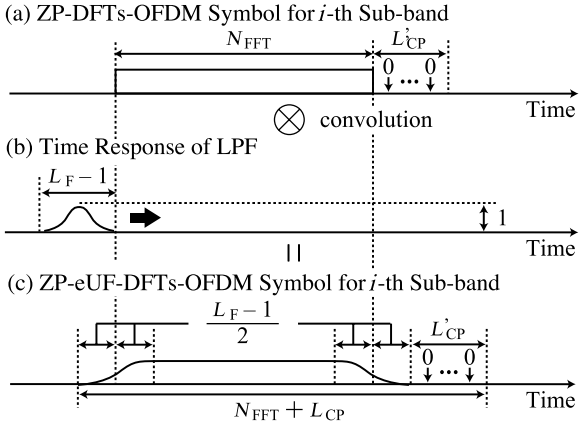

Fig. 5 Generation process of proposed ZP-eUF-DFTs-OFDM symbol in each sub-band.

3.1.2 Receiver Architecture

Figure 6 shows the reception process of the proposed ZP-eUF-DFTs-OFDM. Firstly, an overlap and add (OLA) process [13] shown in Fig. 7 is executed to the k-th reception symbol of the proposed ZP-eUF-DFTs-OFDM $\boldsymbol{r}_k^{\mathrm{ZP(eUF)}} \in \mathbb{C}^{(N_{\mathrm{FFT}}+L_{\mathrm{CP}})\times 1}$ in time-domain. In other words, the end part of the received symbol with a length of $L'_{\mathrm{CP}} + L_{\mathrm{F}} - 1$ ($= L_{\mathrm{CP}}$) is added to the beginning part. Secondly, N_{FFT}-points FFT is performed, and M subcarriers in the allocated band are extracted. Therefore, the received subcarriers (i.e., input frequency-domain subcarriers to channel equalizer) $\boldsymbol{y}_k^{\mathrm{ZP(eUF)}} \in \mathbb{C}^{M\times 1}$ can be expressed as follows:

$$\boldsymbol{y}_k^{\mathrm{ZP(eUF)}} = \boldsymbol{R}_{\mathrm{ZP(eUF)}} \boldsymbol{r}_k^{\mathrm{ZP(eUF)}}, \tag{19}$$

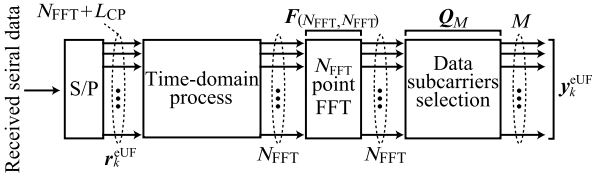

Fig. 6 Reception process of the proposed ZP/CP-eUF-DFTs-OFDM.

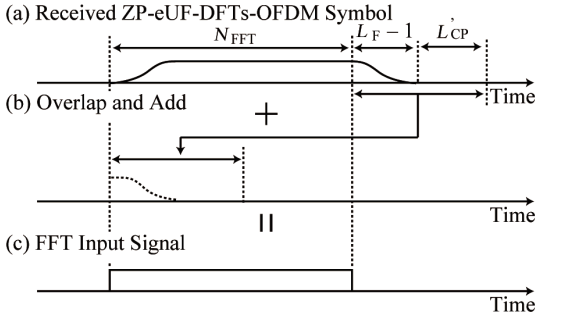

Fig. 7 OLA process at the receiver of the proposed ZP-eUF-DFTs-OFDM.

$$\boldsymbol{R}_{\mathrm{ZP(eUF)}} = \boldsymbol{Q}_M \boldsymbol{F}_{(N_{\mathrm{FFT}},N_{\mathrm{FFT}})} \boldsymbol{R}_{\mathrm{OLA}}, \tag{20}$$

$$\boldsymbol{R}_{\mathrm{OLA}} = \begin{bmatrix} \boldsymbol{I}^{N_{\mathrm{FFT}}\times N_{\mathrm{FFT}}} & \boldsymbol{I}^{L_{\mathrm{CP}}\times L_{\mathrm{CP}}} \\ & \boldsymbol{0}^{(N_{\mathrm{FFT}}-L_{\mathrm{CP}})\times L_{\mathrm{CP}}} \end{bmatrix}, \tag{21}$$

$$(\boldsymbol{Q}_M)_{p,q} = \begin{cases} 1\ (p=q=k) \\ 0\ (\mathrm{other}) \end{cases}, \tag{22}$$

where $\boldsymbol{R}_{\mathrm{OLA}} \in \mathbb{C}^{N_{\mathrm{FFT}}\times(N_{\mathrm{FFT}}+L_{\mathrm{CP}})}$ denotes the OLA process. Also, $1 \le k \le M$, $k \in \mathbb{N}$, and $\boldsymbol{Q}_M \in \mathbb{C}^{M\times N_{\mathrm{FFT}}}$ represents the extraction of the allocated M subcarriers. Finally, after FDE by the MMSE filter, the received bit sequence can be obtained by the inverse process of the transmitter.

3.2 Proposed CP-eUF-DFTs-OFDM

3.2.1 Transmitter Architecture

As shown in Fig. 4, the transmission process of the proposed CP-eUF-DFTs-OFDM [9] just replaces the ZP process of ZP-eUF-DFTs-OFDM by the CP insertion. Figure 8 shows the generation process of the CP-eUF-DFTs-OFDM symbol in each sub-band. Firstly, after the time-domain waveform $\boldsymbol{s}_k^i$ is generated by following the same processes of the UF-DFTs-OFDM, the CP with a length of L'_{CP} $(= L_{\mathrm{CP}} - L_{\mathrm{F}} + 1)$ is prefixed to $\boldsymbol{s}_k^i$ before applying the LPF in each sub-band (Fig. 8(a)). After the CP insertion, the rest of the processes is completely same as that of the ZP-eUF-DFTs-OFDM. Therefore, the k-th CP-eUF-DFTs-OFDM symbol $\boldsymbol{s}_k^{\mathrm{CP(eUF)}} \in \mathbb{C}^{(N_{\mathrm{FFT}}+L_{\mathrm{CP}})\times 1}$ can be expressed by using the matrix $\boldsymbol{J}_i^{\mathrm{CP(eUF)}}$ $(= \boldsymbol{G}_i \boldsymbol{T}_{\mathrm{CP}} (\boldsymbol{F}^i_{(N_{\mathrm{FFT}},M_0)})^{-1}) \in \mathbb{C}^{(N_{\mathrm{FFT}}+L_{\mathrm{CP}})\times M_0}$ as follows:

$$\boldsymbol{s}_k^{\mathrm{CP(eUF)}} = \sum_{i=0}^{B-1} \boldsymbol{J}_i^{\mathrm{CP(eUF)}} \boldsymbol{z}_k^i, \tag{23}$$

$$\boldsymbol{T}_{\mathrm{CP}} = \begin{bmatrix} \boldsymbol{0}^{L'_{\mathrm{CP}}\times(N_{\mathrm{FFT}}-L'_{\mathrm{CP}})} & \boldsymbol{I}^{L'_{\mathrm{CP}}\times L'_{\mathrm{CP}}} \\ & \boldsymbol{I}^{N_{\mathrm{FFT}}\times N_{\mathrm{FFT}}} \end{bmatrix}, \tag{24}$$

where $\boldsymbol{T}_{\mathrm{CP}} \in \mathbb{C}^{(N_{\mathrm{FFT}}+L'_{\mathrm{CP}})\times N_{\mathrm{FFT}}}$ denotes the process of CP insertion. Finally, transmission symbol of the proposed CP-eUF-DFTs-OFDM can be obtained by concatenating successive symbols $\boldsymbol{s}_k^{\mathrm{CP(eUF)}}$. As shown in Fig. 8(c), the CP-eUF-DFTs-OFDM symbol looks very similar to the time-domain windowing-based wave-shaped CP-OFDM or CP-DFTs-OFDM [13], [15]–[17]. In the case of the time-domain windowing-based waveforms, the CP with a length of L_{CP} is attached to the OFDM symbol or the DFTs-OFDM symbol, and then, the time-domain window (e.g., raised-cosine window) is *multiplied* by the CP-attached OFDM or DFTs-OFDM symbol in time-domain. On the other hand, in the case of the proposed CP-eUF-DFTs-OFDM, the time response of an LPF (e.g., Dolph-Chebyshev) is *convoluted* in time-domain as above-mentioned. One of the advantages of the proposed CP-eUF-DFTs-OFDM compared to the time-domain windowing-based schemes is that the frequency response of the LPF can be designed in frequency-domain directly and the effective frequency-domain characteristics of the transmission signal (i.e., OOBE suppression performance) can be easily achieved.

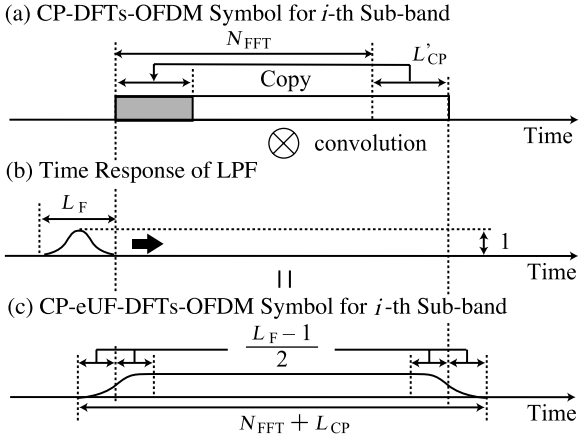

Fig. 8 Generation process of CP-eUF-DFTs-OFDM symbol in each sub-band.

3.2.2 Receiver Architecture

The reception process of the proposed CP-eUF-DFTs-OFDM is same as that of the proposed ZP-eUF-DFTs-OFDM shown in Fig. 6, except for the time-domain process. In the proposed CP-eUF-DFTs-OFDM, the k-th reception CP-eUF-DFTs-OFDM symbol $\boldsymbol{r}_k^{\mathrm{CP(eUF)}} \in \mathbb{C}^{(N_{\mathrm{FFT}}+L_{\mathrm{CP}})\times 1}$ is multiplied by a rectangular window (RW) in time-domain as shown in Fig. 9. This RW multiplication removes the beginning part and end part of the received symbol with a length of L'_{CP} and $L_{\mathrm{F}} - 1$, respectively. Secondly, N_{FFT}-points FFT is performed, and M subcarriers in the allocated band are extracted. Therefore, the received subcarriers (i.e., input frequency-domain subcarriers to channel equalizer) $\boldsymbol{y}_k^{\mathrm{CP(eUF)}} \in \mathbb{C}^{M\times 1}$ can be expressed as follows:

$$\boldsymbol{y}_k^{\mathrm{CP(eUF)}} = \boldsymbol{R}_{\mathrm{CP(eUF)}} \boldsymbol{r}_k^{\mathrm{CP(eUF)}}, \tag{25}$$

$$\boldsymbol{R}_{\mathrm{CP(eUF)}} = \boldsymbol{Q}_M \boldsymbol{F}_{(N_{\mathrm{FFT}},N_{\mathrm{FFT}})} \boldsymbol{R}_{\mathrm{RW}}, \tag{26}$$

$$\boldsymbol{R}_{\mathrm{RW}} = \begin{bmatrix} 0^{N_{\mathrm{FFT}}\times L'_{\mathrm{CP}}} & \boldsymbol{I}^{N_{\mathrm{FFT}}\times N_{\mathrm{FFT}}} & 0^{N_{\mathrm{FFT}}\times(L_F-1)} \end{bmatrix}, \tag{27}$$

where $\boldsymbol{R}_{\mathrm{RW}} \in \mathbb{C}^{N_{\mathrm{FFT}}\times(N_{\mathrm{FFT}}+L_{\mathrm{CP}})}$ denotes the RW multiplication. Finally, after FDE by the MMSE filter, the received bit sequence can be obtained by the inverse process of the

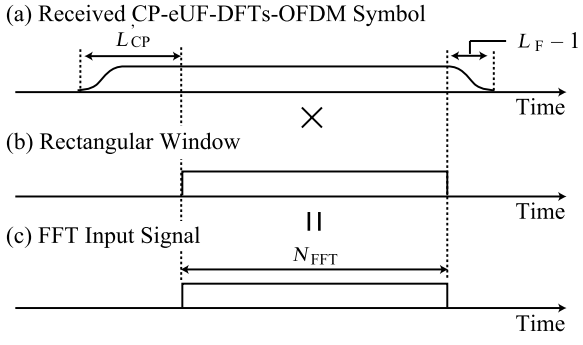

Fig. 9 RW multiplication at the receiver of the proposed CP-eUF-DFTs-OFDM.

transmitter.

3.3 Pre-Distortion Process for the Proposed ZP/CP-eUF-DFTs-OFDM

In the proposed ZP/CP-eUF-DFTs-OFDM, the frequency-domain ripple caused by the LPF can be compensated by the PD process as well as the UF-DFTs-OFDM. A ripple coefficient vector for the proposed ZP/CP-eUF-DFTs-OFDM $\boldsymbol{h}^{\mathrm{X(eUF)}} = [h_1^{\mathrm{X(eUF)}}, h_2^{\mathrm{X(eUF)}}, \ldots, h_M^{\mathrm{X(eUF)}}]^{\mathrm{T}} \in \mathbb{C}^{M\times 1}$ (X $\in$ {ZP, CP}) can be expressed by replacing $\boldsymbol{R}_{\mathrm{UF}}\boldsymbol{J}_{\mathrm{i}}^{\mathrm{UF}}$ with $\boldsymbol{R}_{\mathrm{X(eUF)}}\boldsymbol{J}_{i}^{\mathrm{X(eUF)}}$ in Eq. (16). Thus, when $\boldsymbol{h}_{\mathrm{inv}}^{\mathrm{X(eUF)}}$ is defined as vector $[1/h_1^{\mathrm{X(eUF)}}, 1/h_2^{\mathrm{X(eUF)}}, \ldots, 1/h_M^{\mathrm{X(eUF)}}]^{\mathrm{T}} \in \mathbb{C}^{M\times 1}$, the PD process can be executed by the multiplication of z_{k} and the diagonal matrix $\boldsymbol{H}_{\mathrm{LPF}}^{\mathrm{X(eUF)}}$ (= diag($\boldsymbol{h}_{\mathrm{inv}}^{\mathrm{X(eUF)}}$)) $\in \mathbb{C}^{M\times M}$. Therefore, in the case of the proposed ZP/CP-eUF-DFTs-OFDM wave-shaping with the PD process, z_k should be replaced with $\hat{z}_k = \boldsymbol{H}_{\mathrm{LPF}}^{\mathrm{X(eUF)}} z_k$ in Eq. (3).

3.4 Differences between ZP-eUF-DFTs-OFDM and CP-eUF-DFTs-OFDM

From the viewpoint of generation process of transmission symbol at the transmitter, the ZP-eUF-DFTs-OFDM is slightly inferior to the CP-eUF-DFTs-OFDM with regard to the following points. Firstly, a completely non-signal state in time-domain (i.e., ZP process) for the ZP-eUF-DFTs-OFDM is still challenging in an analog circuit due to the dynamic range limitation of some analog components. Secondly, PAPR of the ZP-eUF-DFTs-OFDM transmission symbol is higher than that of the CP-eUF-DFTs-OFDM transmission symbol because the average transmission power of the ZP-eUF-DFTs-OFDM is reduced by the partial non-signal state. Therefore, the CP-eUF-DFTs-OFDM is relatively superior to the ZP-eUF-DFTs-OFDM.

4. Computer Simulation

To analyze the proposed ZP/CP-eUF-DFTs-OFDM, the characteristics of OOBE, PAPR, and BLER were evaluated by computer simulation with the LTE uplink parameters shown in Table 1. As a channel model, the 3GPP ETU model [20] with a maximum Doppler frequency of 70 Hz at 2.5 GHz was applied for assuming a long-delay multipath fading environment. Therefore, to mitigate the effect of frequency selective fading caused by long-delay multipaths, the extended CP mode (i.e., CP length = 16.7 μs) was used. Therefore, the filter length for the conventional UF-DFTs-OFDM was set to be the same as the CP length in the extended CP mode of LTE (i.e., L_{F} = 129). On the other hand, to avoid the effect of a large frequency-domain ripple caused by longer filter length, the filter length for the proposed eUF-DFTs-OFDM was set to be the same as the CP length in the normal CP mode of LTE (i.e., CP length = 4.7 μs and L_{F} = 37). Also, the number of sub-bands was set to be the same as the number of PRBs per slot (i.e., B = 25) [13].

Table 1 Specifications of transmission signal.

Parameter	Value
Bandwidth	5.0 MHz
Sampling frequency	7.68 MHz
FFT size N_{FFT}	512
DFT size M	300
GI length L_{CP}	128
Number of slots per sub-frame	2
Number of PRBs per slot (= Number of sub-band B)	25
Number of symbols per slot	6 (Extended CP mode)
Filter scheme	Dolph-Chebyshev
Filter length L_{F}	Proposed ZP/CP-eUF-DFTs-OFDM: 37 UF-DFTs-OFDM: 129
Side-lobe attenuation	40 dB

Hereinafter, the proposed ZP-eUF-DFTs-OFDM with and without the PD process are named as *the ZP-eUF scheme (w/ PD)* and *the ZP-eUF scheme (w/o PD)*, respectively, and the proposed CP-eUF-DFTs-OFDM with and without the PD process are named as *the CP-eUF scheme (w/ PD)* and *the CP-eUF scheme (w/o PD)*, respectively. Furthermore, the conventional UF-DFTs-OFDM with and without the PD process and the CP-DFTs-OFDM are named as *the UF scheme (w/ PD)*, *the UF scheme (w/o PD)*, and *the CP scheme*, respectively.

4.1 OOBE Suppression Performance

The OOBE reduction performance was evaluated by the max-hold plot of the relative power spectrum density (PSD) with the transmission signal parameters shown in Table 1. Figure 10 shows relative PSD of the ZP-eUF schemes, the CP-eUF schemes, the UF schemes, and the CP scheme. Note that the resolution bandwidth and the oversampling factor were set to 100 kHz and four, respectively.

The ZP/CP-eUF schemes can improve the OOBE at the channel-edge of the occupied bandwidth (OBW) by 22.5 dB compared to the CP scheme regardless of the PD process

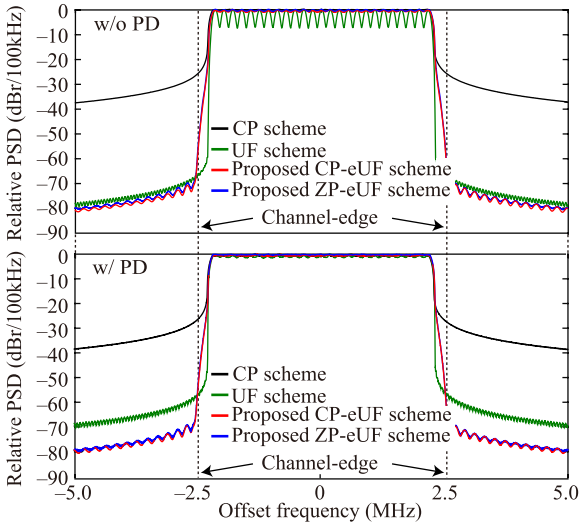

Fig. 10 Relative PSD characteristics.

because the discontinuity between successive transmission symbols is drastically mitigated by the LPF convolution. On the contrary, the OOBE reduction performance of the UF scheme (w/ PD) is inferior to that of the UF scheme (w/o PD) by about 8 dB. The PD process can compensate the attenuated amplitude of subcarriers (i.e., can flatten the ripple caused by the LPF) by amplifying the edge parts of the OBW. This means that the UF scheme induces the large amplification at the edge of the OBW due to the LPF with a quite long length ($L_{\mathrm{F}} = 129$) and drastically degrades the OOBE, while the sufficiently short LPF length ($L_{\mathrm{F}} = 37$) in the proposed ZP/CP schemes barely affects the OOBE.

4.2 PAPR Performance

In this section, the PAPR characteristics of the proposed schemes are evaluated by the complementary cumulative distribution function (CCDF). The PAPR of transmission symbol $x(n)$ is defined as

$$PAPR = \max\left[|x(n)|^2\right] / \mathrm{E}\left[|x(n)|^2\right], \tag{28}$$

where E[·] denotes the expected value. Here, the CCDF of the PAPR exceeding an arbitrary threshold $PAPR_0$ can be defined as

$$\mathrm{CCDF} = \Pr\left[PAPR > PAPR_0\right], \tag{29}$$

where Pr[·] denotes the probability. In general, low PAPR characteristics of the transmission symbol is important to avoid the significant distortion caused by a non-linear power amplifier.

To confirm the PAPR performance of the ZP-eUF schemes and the CP-eUF schemes, CCDF curves of the PAPR for QPSK was simulated and compared with the conventional schemes as shown in Fig. 11. Firstly, the cases without the PD process are discussed. The PAPR characteristics of the UF scheme, the CP-eUF scheme, and the ZP-eUF scheme are degraded compared to the CP scheme

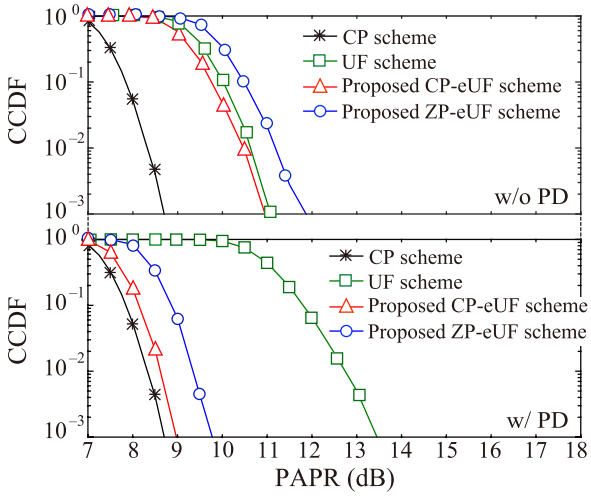

Fig. 11 CCDF curves of PAPR.

by about 2.4 dB, 2.3 dB, and 3.2/ dB, respectively, because the average power of the transmission symbols is reduced by smoothing transmission symbol edges. The PAPR of the UF scheme is worse than the CP-eUF scheme by 0.1 dB because the transition time of the LPF in the UF scheme is longer than that in the CP-eUF scheme. Although the same LPF is used for both schemes, the PAPR of the ZP-eUF scheme is worse than the CP-eUF scheme by 0.8 dB because the transmission symbol of the ZP-eUF scheme includes zero periods (i.e., non-signal state) with a length of L'_{CP} as shown in Fig. 5.

By applying the PD process, the PAPR of the UF scheme is degraded by about 2.5 dB, while the PAPR of the ZP/CP-eUF scheme can be improved by about 2 dB. As mentioned in Sect. 4.1, the PD process impairs the compensation of the ripple derived from the LPF. In other words, the PD process basically averages the amplitude in time-domain but amplifies the attenuated amplitude during the transition time of the LPF. Therefore, in the case of the UF scheme, the attenuated amplitude is amplified drastically during the quite long transition time of the LPF, and thus, the peak power is enhanced. On the other hand, in the case of the ZP-eUF and CP-eUF schemes, the amplification of the attenuated amplitude is trivial because of the short transition time of the LPF ($L_{\mathrm{F}} = 37$). Moreover, the peak power is reduced by averaging the amplitude in the entire time-domain with applying the PD process, resulting in the improvement of PAPR.

4.3 Communication Quality

To ensure high communication quality of the ZP-eUF schemes and the CP-eUF schemes, BLER characteristics were evaluated by applying the additional parameters shown in Table 2. Here, it was assumed that one transport block was allocated to one sub-frame, and all PRBs were occupied by one user. At the receiver, channel variations attributed to multipath fading were estimated by linear interpolation and extrapolation by using reference signals. After the channel estimation, FDE by the MMSE filter was executed for compensating channel variations.

4.3.1 BLER Characteristics

Figure 12 shows BLER characteristics as a function of E_{S}/N_0 for QPSK, 16QAM, and 64QAM. Firstly, we discuss the results without the PD process. The E_{S}/N_0 to

Table 2 Parameters for BLER characteristics evaluation.

Parameter	Value
Modulation, Coding rate	QPSK, $R = 0.59$ 16QAM, $R = 0.54$ 64QAM, $R = 0.55$
Channel coding scheme	Convolutional turbo coding
Number of available REs	3,000
Decoding scheme	Max-Log-MAP algorithm
Decoding iteration	5
Max Doppler frequency	70 Hz
Channel model	3GPP Extended Typical Urban [20]

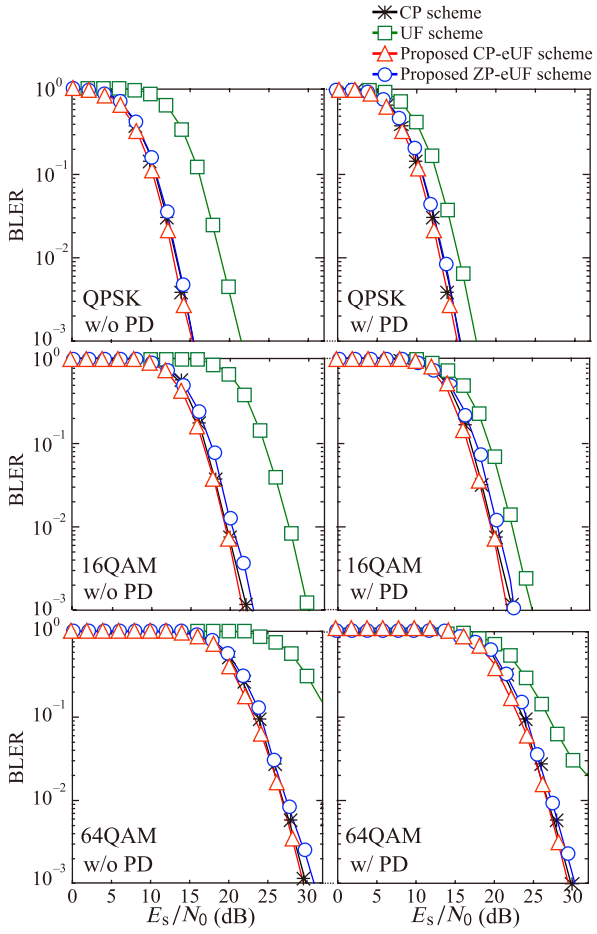

Fig. 12 BLER characteristics.

achieve BLER = 10^{-3} of the UF-scheme is degraded by 6 dB or more compared to the CP-scheme because of the frequency-domain ripple caused by the long filter length. On the other hand, the CP-eUF scheme can improve the E_S/N_0 to achieve BLER = 10^{-3} by about 6 dB and 8 dB for QPSK and 16QAM, respectively, compared to the UF scheme. Furthermore, the error floor was eliminated for 64QAM, resulting in the same communication quality as the CP scheme. Also, the ZP-eUF scheme can improve the E_S/N_0 to achieve BLER = 10^{-3} by about 6 dB and 7 dB for QPSK and 16QAM, respectively, compared to the UF scheme, and the error floor was eliminated for 64QAM.

Secondly, we discuss the results with the PD process. The UF scheme (w/ PD) can improve the E_S/N_0 to achieve BLER = 10^{-3} of the UF scheme (w/o PD) by about 3.5 dB and 5 dB for QPSK and 16QAM, respectively. However, these BLER characteristics of the UF scheme (w/ PD) are still remarkably inferior to those of the ZP/CP-eUF schemes.

These results indicate that the LPF with a quite short length for the ZP/CP-eUF schemes (i.e., $L_F = 37$) sufficiently reduces the frequency-domain ripple caused by the long filter length for the UF scheme (i.e., $L_F = 129$), and the power depression of the received subcarriers is mitigated in the ZP/CP-eUF schemes. In addition, the E_S/N_0 to achieve BLER = 10^{-3} of the ZP-eUF schemes are inferior to that of the CP-eUF schemes by about 1 dB for 16QAM and 64QAM because OLA process shown in Fig. 7 induces the extra noise components to the received symbols.

5. Conclusion

In this paper, we proposed eUF-DFTs-OFDM that applies the LPF with a quite short length in combination with the ZP or CP to improve the communication quality of the conventional UF-DFTs-OFDM in a long-delay multipath environment. To confirm the usefulness of the proposed eUF-DFTs-OFDM, the characteristics of OOBE, PAPR, and BLER were numerically evaluated by computer simulation. The evaluation results indicated that the proposed ZP/CP-eUF schemes achieved higher OOBE reduction while maintaining the same level of PAPR and communication quality as the CP scheme even in a long-delay multipath environment.

Acknowledgments

A part of this research was conducted under a contract of R&D for Expansion of Radio Wave Resources, organized by the Ministry of Internal Affairs and Communications, Japan.

References

[1] S. Chen and J. Zhao, "The requirements, challenges, and technologies for 5G of terrestrial mobile telecommunication," IEEE Commun. Mag., vol.52, no.5, pp.36–43, May 2014.
[2] ITU-R, "IMT Vision - Framework and overall objectives of the future development of IMT for 2020 and beyond," Recommendation M.2083-0, Sept. 2015.
[3] ITU, "IMT-2020," ITU, Technical Report, 2017.
[4] G. Wunder, P. Jung, M. Kasparick, T. Wild, F. Schaich, Y. Chen, S. Brink, I. Gaspar, N. Michailow, A. Festag, L. Mendes, N. Cassiau, D. Ktenas, M. Dryjanski, S. Pietrzyk, B. Eged, P. Vago, and F. Wiedmann, "5GNOW: Non-orthogonal, asynchronous waveforms for future mobile applications," IEEE Commun. Mag., vol.52, no.2, pp.97–105, Feb. 2014.
[5] P. Banelli, S. Buzzi, G. Colavolpe, A. Modenini, F. Rusek, and A. Ugoliniet, "Modulation formats and waveforms for the physical layer of 5G wireless networks: Who will be the heir of OFDM?," IEEE Signal Process. Mag., vol.31, no.6, pp.80–93, Nov. 2014.
[6] A. Farhang, N. Marchetti, F. Figueiredo, and J.P. Miranda, "Massive MIMO and waveform design for 5th generation wireless communication systems," Proc. Int. Conf. on 5G for Ubiquitous Connectivity, pp.70–75, Nov. 2014.
[7] A.A. Zaidi, R. Baldemair, H. Tullberg, H. Bjorkegren, L. Sundstrom, J. Medbo, C. Kilinc, and I.D. Silva, "Waveform and numerology to support 5G services and requirements," IEEE Commun. Mag., vol.54, no.11, pp.90–98, Nov. 2016.
[8] F. Schaich, T. Wild, and Y. Chen, "Waveform contenders for 5G-suitability for short packet and low latency transmission," Proc. IEEE 79th VTC, pp.1–5, May 2014.
[9] Y. Mizutani, H. Kuriki, Y. Kodama, K. Mizutani, T. Matsumura, and H. Harada, "Enhanced universal filtered-DFTs-OFDM for long-delay multi-path environment," Proc. PIMRC2017, pp.1–6, Oct. 2017.
[10] H. Kuriki, K. Mizutani, and H. Harada, "Enhanced UF-OFDM for large delay spread channel," Proc. IEICE General Conf., B-5-34,

March 2016 (in Japanese).
[11] H. Kuriki, K. Mizutani, T. Matsumura, and H. Harada, "Enhanced UF-OFDM for long-delay multipath fading environment," Proc. IEEE VTC 2017-Spring, pp.1–5, June 2017.
[12] LG Electronics, "Flexible CP-OFDM with variable ZP," 3GPP TSG-RAN WG1 #84bis, R1-162516, April 2016.
[13] Qualcomm Inc., "Waveform candidates," 3GPP TSG-RAN WG1 #84bis, R1-162199, April 2016.
[14] J.B. Dore, R. Gerzaguet, and D. Ktenas, "5G cellular networks with relaxed synchronization: Waveform comparison and new results," Proc. VTC 2016-Spring, pp.1–6, May 2016.
[15] K. Mizutani, Z. Lan, and H. Harada, "Time-domain windowing design for IEEE 802.11af based TVWS-WLAN systems to suppress out-of-band emission," IEICE Trans. Commun., vol.E97-B, no.4, pp.875–885, April 2014.
[16] R. Funada, K. Mizutani, and H. Harada, "Wireless transmitter, wireless receiver, wireless transmission method, and wireless reception method," Patent no.: US 9,450,800 B2, Sept. 20, 2016 (Submission Jan. 2013).
[17] Y. Kodama, K. Mizutani, T. Matsumura, and H. Harada, "LTE uplink system based on universal time-domain windowed DFTs-OFDM," Proc. WPMC 2017, pp.1–6, Dec. 2017.
[18] D. Galda and H. Rohling, "A low complexity transmitter structure for OFDM-FDMA uplink systems," Proc. IEEE VTC Spring 2002, pp.1731–1741, May 2002.
[19] F. Hasegawa, S. Shinjo, A. Okazaki, A. Okamura, L. Brunel, and D. Mottier, "Static sequence assisted out-out-of-band power suppression for DFT-s-OFDM," Proc. IEEE PIMRC2015, pp.61–65, Sept. 2015.
[20] 3GPP, "Base Station (BS) radio transmission and reception (Release 8)," 3GPP TS 36.104, May 2008.

Yuji Mizutani received a B.E. degree in electric and electrical engineering and an M.E. degree in informatics from the Kyoto University, Japan in 2017 and 2019, respectively. He currently researches the topics of physical layers of the beyond 5 th generation mobile communication (5G) system.

Hiroto Kuriki received a B.E. degree in electric and electrical engineering and an M.E. degree in informatics from the Kyoto University, Japan in 2016 and 2018, respectively. He currently researches the topics of physical layers of the beyond 5th generation mobile communication (5G) system.

Yosuke Kodama received a B.E. degree in electric and electrical engineering and an M.E. degree in informatics from the Kyoto University, Japan in 2016 and 2018, respectively. He currently researches the topics of physical layers of the beyond 5th generation mobile communication (5G) system.

Keiichi Mizutani is an assistant professor of Kyoto University. He received a B.E. degree in electric, electrical and system engineering from the Osaka Prefecture University, in 2007, and an M.E. and Ph.D. degree in electric and electrical engineering from the Tokyo Institute of Technology, in 2009 and 2012, respectively. He was an invited researcher at Fraunhofer Heinrich Hertz Institute, Germany, in 2010. From April 2012 to Sept. 2014, he was a researcher at NICT. He currently researches the topics of physical layer technologies in white space communications, dynamic spectrum access, and the 5G and Beyond 5G access technologies. He received the Special Technological Award and Best Paper Award from IEICE SR technical committee in 2009 and 2010 respectively, the Young Researcher's Award from IEICE SRW technical committee in 2016, and WPMC 2017 Best Paper Award. Dr. Mizutani is a member of the IEEE.

Takeshi Matsumura was an associate professor of Kyoto University. Now, he is a research manager at NICT, and he has been also a researcher of Kyoto University. He received the M.S. degree in Electronics Engineering in 1998 and Ph.D. in Nano-mechanics Engineering in 2010, from Tohoku University. During 1998–2007, he had been engaged in the R&D of wireless communications devices in some companies. In April 2007, he joined NICT as a researcher and engaged in whitespace communication systems, and 5G mobile communication systems. During 2016–2019, he engaged in baseband signal processing, whitespace communication systems, and 5G as an associate professor in Kyoto University. His research interests include white-space communication systems, wide-area wireless network systems, and 5G and Beyond 5G mobile communication systems. Dr. Matsumura is a member of the IEEE.

Hiroshi Harada is a professor of Kyoto University. He joined the Communications Research Laboratory, Ministry of Posts and Communications, in 1995 (currently NICT) and has worked for NICT for 19 years. He was a post doctoral fellow of Delft University of Technology, The Netherlands from 1996 to 1997. He has joined several international standardization committees and forums on Software Defined Radio (SDR), cognitive radio, white space, wireless regional area network and Wireless IoT in the United States as well as in Japan and fulfilled important roles. He served as the vice chair of IEEE 802.15.4g, IEEE 802.15.4m, IEEE 1900.4, TIA TR-51 and the chair of IEEE Dyspan Standards Committee. He also served as in the board of directors of the SDR Forum, WhiteSpace Alliance, and Dynamic Spectrum Alliance. He is a Founder of the Wi-SUN Alliance, and has served as the chair of the board of the alliance since 2012. He moreover was the chair of the IEICE Technical Committee on Software Radio (TCSR) in 2005–2007 and has been the chair of Public Broadband Mobile Communication Development Committee, ARIB since 2010. He is the author of Simulation and Software Radio for Mobile Communications (Artech House, 2002). He received fellow of IEICE in 2006, and also received the achievement awards of IEICE in 2009 and 2018, respectively, on the topic of cognitive radio and wireless smart metering systems.